Spontaneous generation of inertia–gravity wave packets by balanced geophysical flows

By ÁLVARO VIÚDEZ[1] AND DAVID G. DRITSCHEL[2]

[1]Institut de Ciènces del Mar, CSIC, Barcelona, Spain
aviudez@cmima.csic.es

[2]School of Mathematics and Statistics, University of St Andrews, St Andrews, UK
dgd@mcs.st-and.ac.uk

The generation and propagation of a packet of small-amplitude inertia–gravity waves (IGWs) in a rotating stratified balanced flow is described. The initially balanced geophysical flow is an unstable baroclinic jet which breaks up into a street of cyclonic and anticyclonic vortices. The small-amplitude unbalanced component of the flow is extracted from the large-amplitude mesoscale balanced flow using the optimal potential vorticity balance approach. This analysis reveals that during the instability the balanced flow spontaneously emits bursts of IGWs. The emission occurs along two directions, into and out of the anticyclonic vortices. The inward-waves remain trapped inside the vortices while the outward-waves propagate away from them as a packet of small-amplitude IGWs with a three-dimensional helical structure. The wave packet emission is confirmed for different spatial resolutions (128^3, 160^3, 192^3 and 256^3 grid points). The ratio between the balanced vertical and horizontal velocity components is of the order of 10^{-3}, as is typical of mesoscale geophysical flows. The ratio between the unbalanced vertical and horizontal components is about 0.1. Since the unbalanced horizontal and the balanced vertical velocity components are of similar magnitude, the vertical velocity of the IGWs is about 10^{-4} times the balanced horizontal velocity. The IGWs are dominated by frequencies close to the inertial frequency and have a clockwise-rotating horizontal velocity, similar to plane wave solutions.

1. Introduction

There are many indications that atmospheric and oceanic flows characterized by an $O(1)$ Rossby number and initially in a state of 'balance' – here meaning a hypothetical state void of inertia–gravity waves (IGWs) – cannot remain that way owing to the spontaneous generation of small-amplitude IGWs (Lorenz & Krishnamurthy 1987; Bokhove & Shepherd 1996; Camassa & Tin 1996; Warn 1997; Ford, McIntyre & Norton 2000; Plougonven & Zeitlin 2002; Plougonven, Teitelbaum & Zeitlin 2003; Vanneste & Yavneh 2004; Vanneste 2004). At $O(1)$ Rossby numbers, however, there is no consensus on the exact meaning of the terms geostrophic adjustment, Lighthill emission, and spontaneous-adjustment emission (SAE; see Ford *et al.* 2000; Saujani & Shepherd 2002). The term SAE is used here to refer to the spontaneous generation of IGWs that we analyse. The precise mechanisms controlling this SAE are, also, not well understood. In particular, what are the balanced flow features which most favour SAE?

Observing and simulating SAE has been the subject of intense research activity. IGW emission in baroclinic jets, such as found near the atmospheric tropopause, has been simulated numerically using two-dimensional hydrostatic (Griffiths & Reeder 1996) and non-hydrostatic (Snyder, Skamarock & Rotunno 1993) models. Three-dimensional simulations (permitting baroclinic instability) have been carried out using the hydrostatic (O'Sullivan & Dunkerton 1995), non-hydrostatic and compressible (Zhang 2004), and anelastic (Lane *et al.* 2004) approximations. In most cases, the IGWs were inferred from the divergence of the horizontal velocity. A main difficulty in the numerical simulation of SAE is to reproduce, within an IGW-permitting model (allowing the generation of IGWs, as opposed to the quasi- or semi-geostrophic model) a time-dependent but otherwise very well balanced geophysical flow (i.e. free of IGWs). Once one SAE event is identified, a second difficulty consists of extracting, diagnostically, the typically small IGW fields from the large balanced fields, that is, isolating the unbalanced component of the flow. Since these IGWs are of small amplitude, these two difficulties primarily concern the exactness of the dynamical theory and the precision of both the numerical model and the IGW extraction approach.

In this paper, we describe a particular way of producing SAE by a balanced flow. The initially balanced flow is an unstable baroclinic jet which breaks up into a street of cyclonic and anticyclonic vortices (§ 2.1). During this instability, SAE occurs both within and along the exterior flank of one of the developing anticyclones, resulting in trapped IGWs within the vortex and a packet of IGWs propagating away. This generation first appears as anomalies in the total vertical velocity and proves robust for widely different grid resolutions (§ 2.2). The balanced and unbalanced (IGW) fields are then separated from the total fields using the optimal potential vorticity balance approach (§ 2.3). This analysis determines the unbalanced three-dimensional velocity and the vertical displacement of isopycnals, clearly revealing the generation and propagation of the wave packet and trapped waves.

2. The spontaneous generation

2.1. *The total flow*

The instability of a three-dimensional (baroclinic) jet is simulated using a triply periodic non-hydrostatic numerical model (Dritschel & Viúdez 2003) initialized using the potential vorticity (PV) initialization approach (Viúdez & Dritschel 2003). The PV is represented by contours lying on isopycnal (constant density) surfaces. The state variables are the components of the vector potential $\boldsymbol{\varphi} = (\varphi, \psi, \phi)$ which provide the velocity $\boldsymbol{u}$ (proportional to $\nabla \times \boldsymbol{\varphi}$) and the vertical displacement of isopycnals $\mathscr{D}$ (proportional to $\nabla \cdot \boldsymbol{\varphi}$).

The flow evolution in the reference simulation, after an initialization procedure designed to balance the small initial perturbation, is shown in figure 1 for the PV anomaly field $\varpi \equiv \Pi - 1$, where Π is the dimensionless total PV. In this reference simulation we use a 128^3 grid in a domain of vertical extent $L_Z = 2\pi$ (which defines the unit of length) and horizontal extents $L_X = L_Y = cL_Z$, where $c \equiv 10$ is the ratio of the mean Brunt–Väisälä to Coriolis frequency $c \equiv N/f$. We take the (mean) buoyancy period (b.p.) as the unit of time by setting $N \equiv 2\pi$. One inertial period (i.p.) equals 10 b.p. The other parameters are the time step $\delta t = 0.01$, initialization time $\Delta t_I = 5$ i.p., and extreme values of the PV anomaly $\varpi = \{-0.75, 0.75\}$. The initialization time is the minimum time required for the fluid to reach its initial perturbed state with minimal
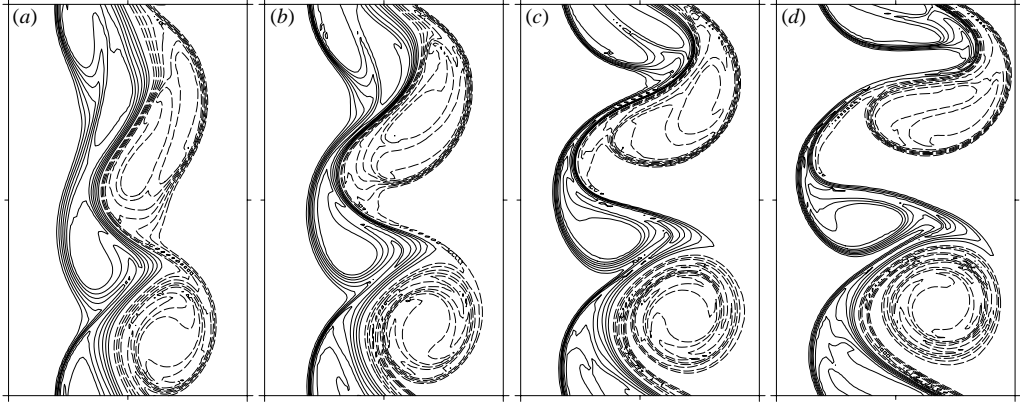
FIGURE 1. Horizontal distributions of PV anomaly ϖ at $z = 0$ at times (a) $t = 6$, (b) $t = 7$, (c) $t = 8$, and (d) $t = 9$ i.p.. Contour interval $\Delta = 0.1$; negative values are dashed (zero contour omitted). Only the relevant part of the domain's x-extent is shown: $x \in [-\pi, \pi]c30/64$, and $y \in [-\pi, \pi]c$.

generation of IGWs. Further details of the three-dimensional jet configuration are given in Viúdez & Dritschel (2004a, b).

The spontaneous-adjustment emission (SAE) occurs after $t = 6$ i.p., so only times $t = 6$, 7, 8 and 9 i.p. are described here. SAE is seen clearly on the eastern side of the developing northern anticyclone ($\varpi < 0$) in figure 1. Over this time interval, the flow has a (local) Rossby number $R_o = \zeta/f \in [-0.71, 0.85]$, where ζ is the vertical vorticity, a maximum Froude number (the magnitude of the horizontal vorticity divided by the total buoyancy frequency) $\max\{F_r\} = 0.43$, a maximum horizontal speed $\max\{|\boldsymbol{u}_h|\} = 2.0$, vertical velocities $w \in [-9.9, 9.9] \times 10^{-3}$, and vertical isopycnal displacements of $\mathscr{D} \in [-0.36, 0.36]$.

2.2. *The generation of an IGW packet*

The flow at $t = 6$ i.p. is very close to a state of balance as deduced from the lack of IGWs in the total vertical velocity w (figure 2a). The w pattern at this stage is consistent with balanced dynamics, and in particular closely matches the quasi-geostrophic (QG) vertical velocity w^q (figure 3a, obtained by solving the QG omega equation, see Viúdez & Dritschel 2004a). The fields of w and w^q do differ, however, since, for large R_o the QG approximation filters a significant part of the balanced flow.

Between $t = 6$ and 7 i.p. a packet of IGWs is observed along the eastern flank of the developing anticyclone in the northern half of the domain. The packet moves eastwards along with the anticyclone's eastern PV edge. The increase in the amplitude of the disturbance from $t = 7$ (figure 2b) to $t = 8$ i.p. (figure 2c), and its decrease at $t = 9$ i.p. (figure 2d) is due to the upward group velocity of the wave packet. The IGW propagation occurs in a localized part of the flow, which remains elsewhere in balance. QG theory overlooks this IGW generation completely (figure 3b).

At $t = 6$ i.p., there is no evidence of the IGW packet in the whole fluid column, as shown in the west–east vertical section of w (figure 4a). Though both the developing cyclone (west) and anticyclone (east) have the same absolute PV anomaly ($\max\{|\varpi|\} = 0.75$), the anticyclone has a larger vertical extent owing to the outward displacement of isopycnals. The upward and eastward propagation of the IGW packet can be clearly identified at subsequent times $t = 7$, 8, and 9 i.p. as anomalies in the
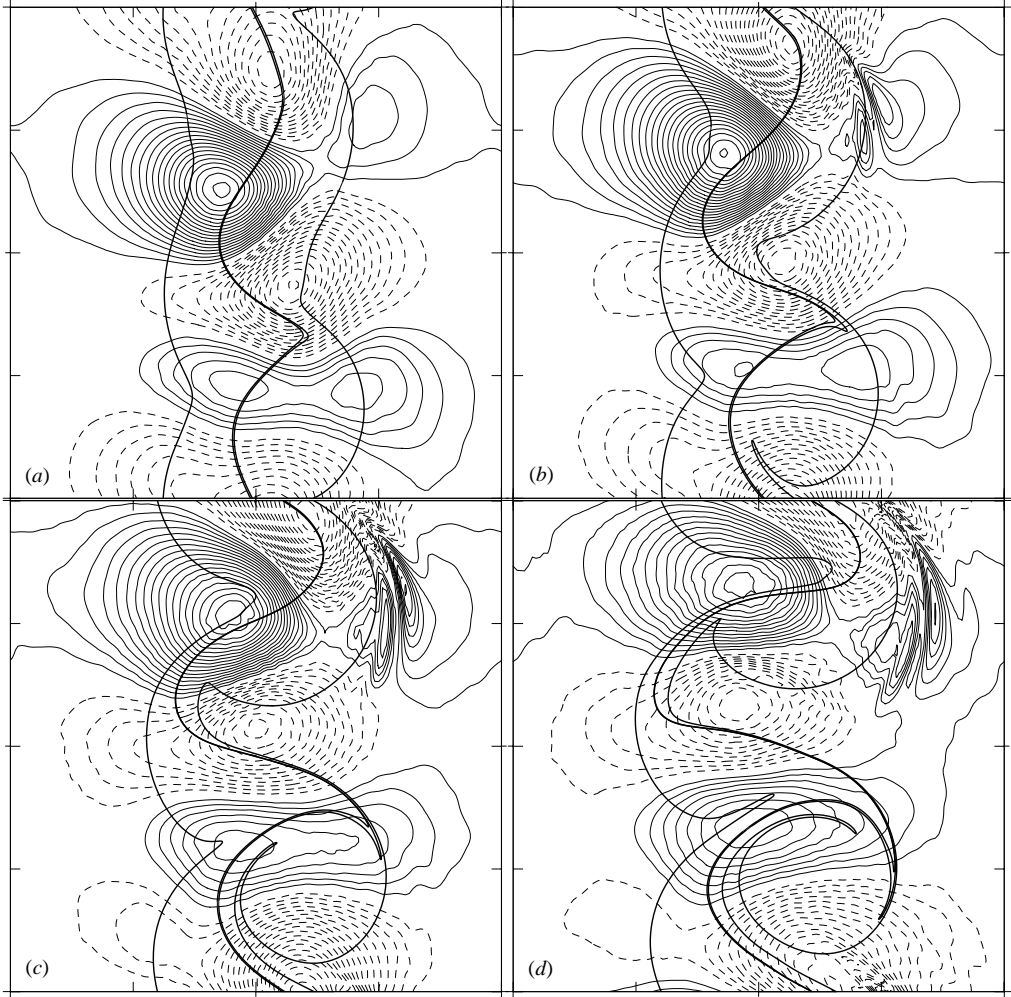
FIGURE 2. Horizontal distributions of w on the plane $z = \pi 28/64$ at (*a*) $t = 6$, (*b*) $t = 7$, (*c*) $t = 8$, and (*d*) $t = 9$ i.p.. Contour interval $\Delta = 5 \times 10^{-5}$; negative values are dashed (zero contour omitted). The outer PV jump at $z = 0$ (thick contour line) is included for reference. The complete horizontal extent is shown $x \in [-\pi, \pi]c$, and $y \in [-\pi, \pi]c$.

region of positive w in the upper half of the eastern anticyclone (figures 4*b*,*c*,*d*). Since the PV distribution of the baroclinic jet is initially vertically symmetric, the fields remain vertically symmetric (or antisymmetric) throughout the jet evolution. Thus, another IGW packet is generated from the lower half of the jet and propagates downwards, in a region of negative w. Some disturbances can be discerned in the interior of the jet as well, but these are difficult to interpret from the total w distributions. Note how a part of the negative PV flow cuts into the positive PV flow during the jet break up (figure 4*d*).

This SAE event is not clearly apparent in lower resolution simulations. At a lower resolution of 64^3 grid points (figure 5*a*), the IGWs are significantly less coherent. Higher resolutions of 160^3, 192^3 and 256^3 grid points (figure 5*b*,*c*,*d*) reproduce the w anomalies of the IGW packet found in the 128^3 case (figure 2*b*). Importantly, the spatial scales within the wave packet are comparable at all these higher resolutions.
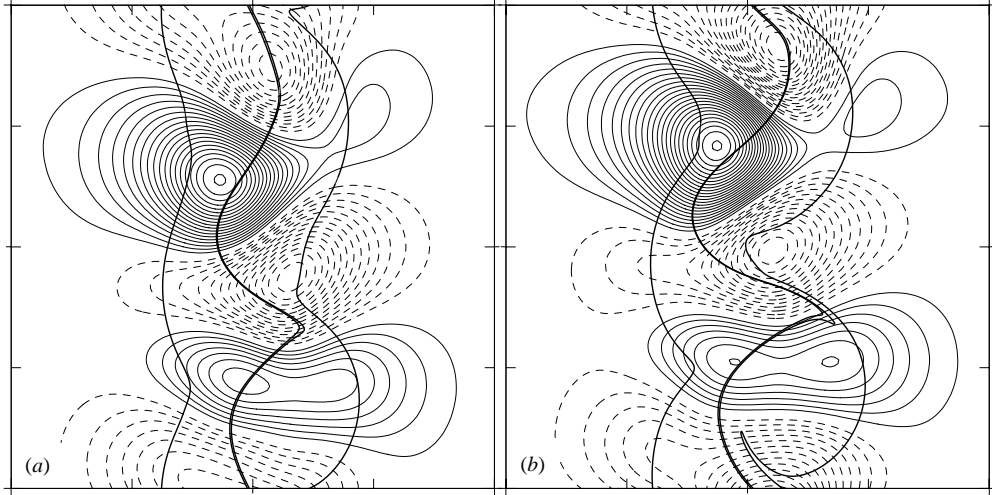
FIGURE 3. Horizontal distributions of the QG vertical velocity w^q at $z = \pi 28/64$ at (*a*) $t = 6$ and (*b*) $t = 7$ i.p.. Contour levels are the same as used in figure 2.
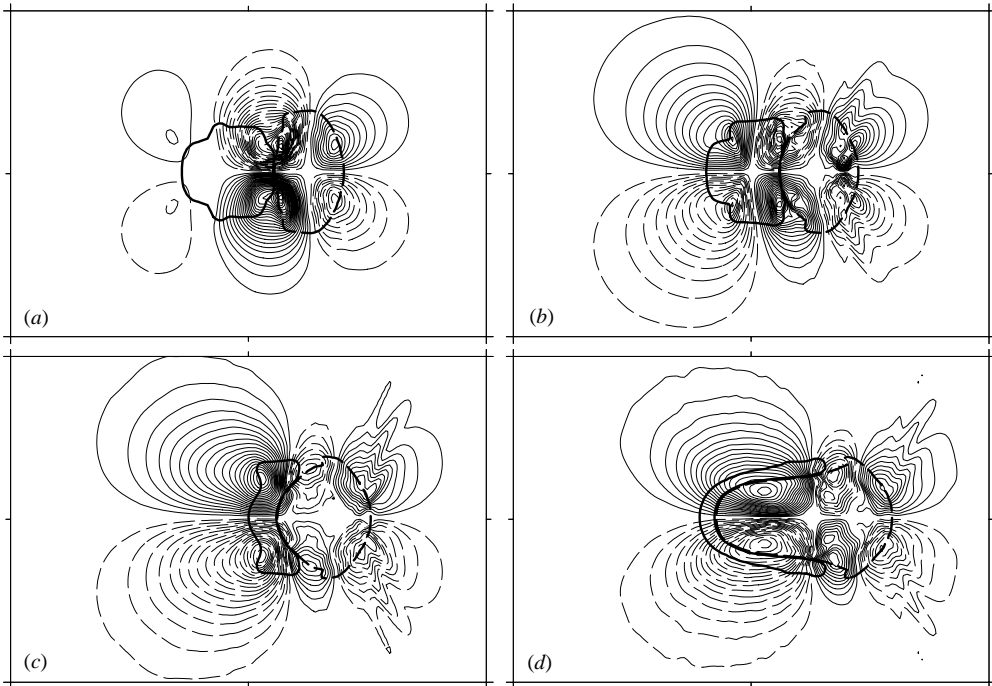

FIGURE 4. Vertical distributions of vertical velocity w on the plane $y = \pi 38/64$ at (*a*) $t = 6$, (*b*) $t = 7$, (*c*) $t = 8$, and (*d*) $t = 9$ i.p.. Contour interval $\Delta = 2 \times 10^{-4}$; negative values are dashed (zero contour omitted). The outer PV contour (thick contour line) is included for reference. Only the vertical range $z \in [-2.15, 2.15]$ is shown with the scale ratio $\Delta_X / \Delta_Z = c$ preserved.

The increase of small-scale perturbations in w with increasing resolution in figure 5 is associated with numerical damping. To avoid the generation of grid-scale noise, a bi-harmonic hyperdiffusion term $-\mu(\nabla_q^4 \mathscr{A}, \nabla_q^4 \mathscr{B})$, where $\nabla_q \chi \equiv (\partial \chi / \partial x, \partial \chi / \partial y, f/N \partial \chi / \partial z)$ is the gradient operator in the vertically stretched space, is added to
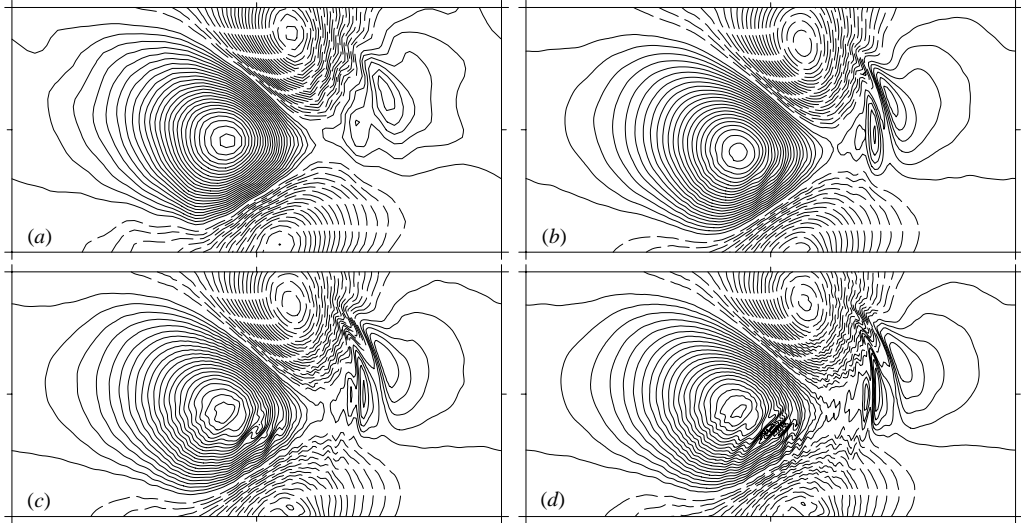
FIGURE 5. Horizontal distributions of w on the plane $z = \pi 28/64$ at $t = 7$ i.p. for simulations with resolutions (*a*) 64^3, (*b*) 160^3, (*c*) 192^3, and (*d*) 256^3 grid points. Contour interval $\Delta = 5 \times 10^{-5}$; negative values are dashed (zero contour omitted). Only the northern half of the domain is shown.
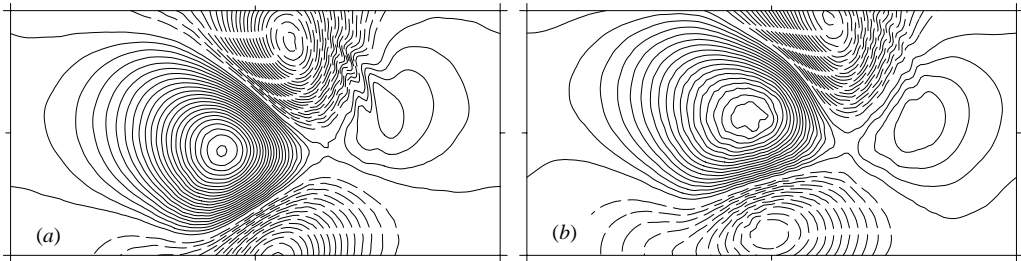

FIGURE 6. Horizontal distributions of the balanced vertical velocity w_{bal} corresponding to figure 5 at (*a*) $t = 7$ i.p. and (*b*) $t = 8$ i.p.

the equations for the rate of change of the horizontal ageostrophic vorticity ($\mathscr{A}, \mathscr{B}$). The hyperviscosity coefficient μ is chosen by specifying the damping rate (*e*-folding, e_f) of the largest wavenumber in spectral space per inertial period. Since $e_f = 50$ is kept constant, independent of the grid size, small-scale features develop with increasing resolution. This, however, does not affect the generation of the IGW packet. Numerical simulations with a larger frequency ratio $c = N/f = 10^2$ reproduced very similar results.

2.3. *The unbalanced flow*

The balanced vector potential of the flow, $\boldsymbol{\varphi}_{bal} = (\varphi_{bal}, \psi_{bal}, \phi_{bal})$, is obtained diagnostically using the optimal PV (OPV) balance approach (Viúdez & Dritschel 2004*c*, Dritschel & Viúdez 2005), and the balanced quantities are derived therefrom. From a given PV field, the OPV balance approach diagnoses a flow, here called the 'balanced flow', having only IGWs which have been spontaneously generated during the process of acquiring its own PV (omitting therefore IGWs due to other processes). The balanced vertical velocity $w_{bal} \equiv (\partial\varphi_{bal}/\partial y - \partial\psi_{bal}/\partial x)/f$ (figure 6) is, to a large extent, free of IGWs as a comparison between figure 6(*a, b*) and figure 2(*b, c*) reveals.
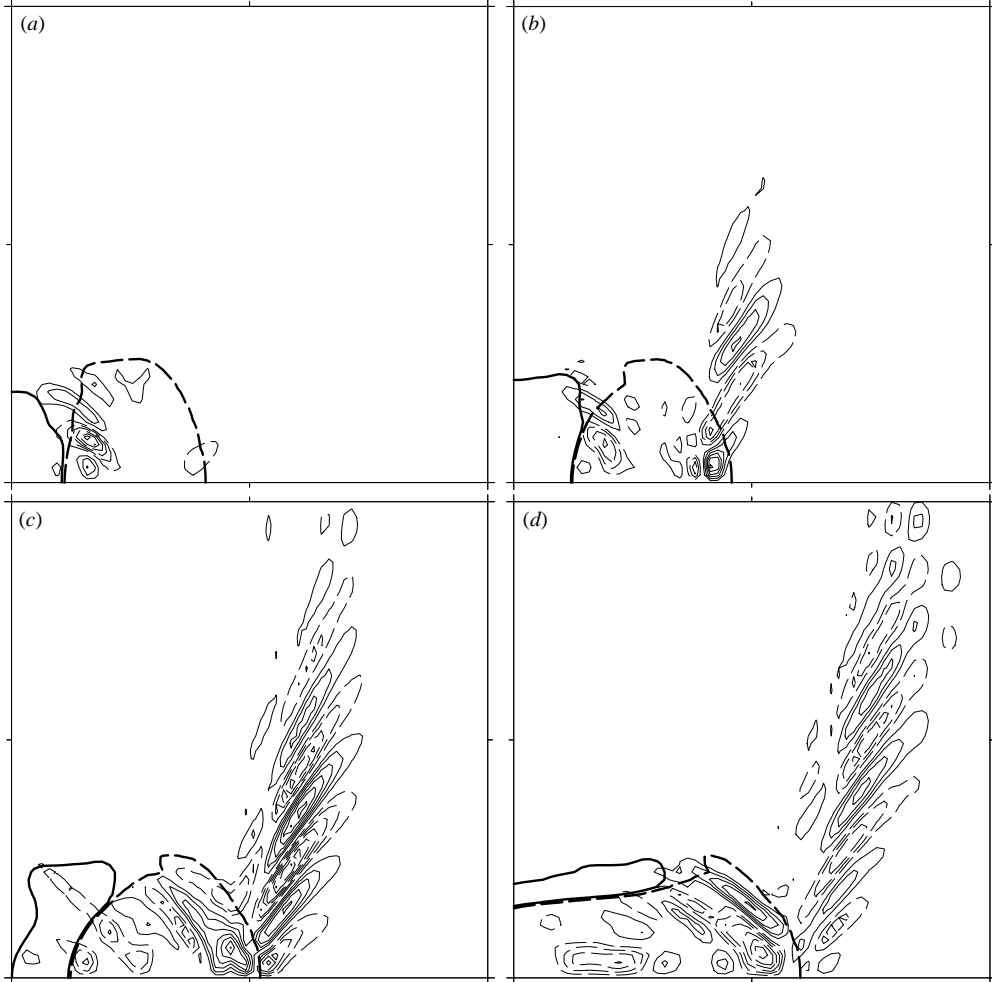
FIGURE 7. Vertical distributions of the unbalanced vertical velocity w_{imb} on the plane $y = \pi 38/64$ at (*a*) $t = 6$, (*b*) $t = 7$, (*c*) $t = 8$, and (*d*) $t = 9$ i.p. Contour interval $\Delta = 5 \times 10^{-5}$; negative values are dashed (zero contour omitted). The outer PV contour (thick contour line) is included for reference. Only the upper-eastern part of the vertical section ($x = [0, \pi]$, $z = [0, \pi]$) is shown. The scale ratio $\Delta_X/\Delta_Z = c$ is preserved.

A small trace of IGWs is still present in figure 6(*a*) because SAE occurs during the time interval required for the anticyclone to spin up in the optimal PV balance procedure. That is, $t = 6$ i.p. (figure 6*a*) is too close to the SAE event. At later times, the trace of the IGW packet in w_{bal} is significantly smaller (figure 6*b*).

The balanced component of the vector potential $\boldsymbol{\varphi}_{bal}$ is then subtracted from the total potential to obtain the unbalanced vector potential $\boldsymbol{\varphi}_{imb} = (\varphi_{imb}, \psi_{imb}, \phi_{imb}) \equiv \boldsymbol{\varphi} - \boldsymbol{\varphi}_{bal}$ from which the unbalanced quantities are derived. The propagation of the IGW packet is clearly seen in the time sequence of the unbalanced vertical velocity $w_{imb} \equiv (\partial \varphi_{imb}/\partial y - \partial \psi_{imb}/\partial x)/f$ (figure 7). At $t = 6$ i.p. (figure 7*a*), there is no unbalanced vertical velocity except for some small waves present inside the jet whose origin is unclear. SAE occurs between $t = 6$ and $t = 7$ i.p., and is clearly visible in figure 7(*b*) as a train of waves moving upward, with the largest amplitudes still located near
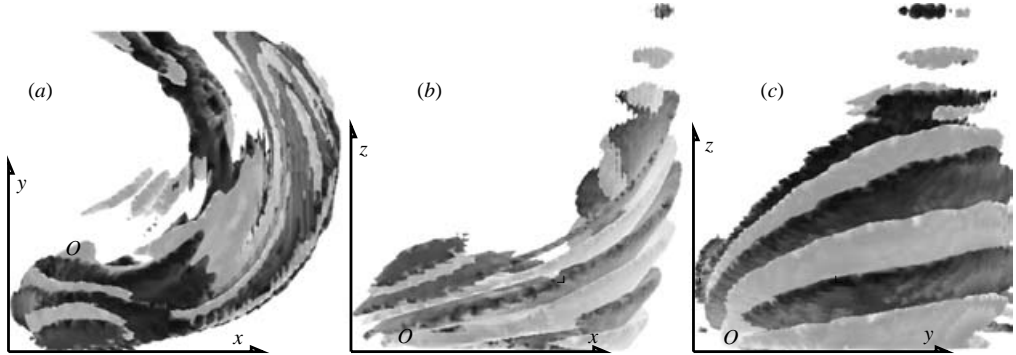
FIGURE 8. Isosurfaces of $w_{imb} = 10^{-4}$ (dark grey) and $w_{imb} = -10^{-4}$ (light grey) at $t = 8$ i.p. in the anticyclone viewed from (*a*) the top, (*b*) south, and (*c*) east. O indicates the origin of the IGW packet.

the base ($z = 0$) of the developing anticyclone. One inertial period later (figure 7*c*) the wave packet has moved upward and eastward, with the largest amplitudes (3×10^{-4}) now located above the anticyclone. Other waves are generated in the opposite direction, with wave phases perpendicular to those in the IGW packet. These waves do not propagate further upward, but are apparently trapped inside the anticyclone. At $t = 8$ i.p. (figure 7*d*), the IGW has continued its upward and eastward propagation, with the w_{imb} maxima now at mid-height. At this stage, the upper waves of the IGW packet reach the upper periodic plane of the computational domain where they exactly cancel with the waves of the antisymmetric wave packet propagating downwards. Thereafter, the counter-propagating waves interfere (noticeable at the top of figure 7*d*). The interior waves remain trapped inside the anticyclone.

The magnitude of the unbalanced vertical velocity (10^{-4}) represents only a very tiny fraction of the total velocity of the flow. The IGWs contribute only 0.01% of the horizontal velocity (which is $O(1)$). Even in this case, the OPV balance procedure is able to extract them unambiguously from the total vertical velocity.

The IGW packet, so far seen in cross-sections, originates in the southern side of the developing anticyclone, where the local rate of change of PV is large. The packet propagates in all three directions, upward and northward along the curved edge of the anticyclone. As a result, the phases form a complex three-dimensional helical structure (figure 8). The phases move downwards (figure 9*a*) completing a vertical displacement of about 0.1π in 5 b.p., i.e. a vertical phase speed $\mathcal{W} \sim 2 \times 10^{-2}\pi$. The local frequency of the waves, as inferred from (figure 9*a*), is $\omega \sim (1/2\,\text{cycles})/(5\,\text{b.p.}) = 0.1\,\text{cycles/b.p.} = f$, i.e. close to the inertial frequency. The vertical angle of the phases is about $45°$ in the stretched QG space ($x, y, Nz/f$), which implies a ratio $m/k \simeq c = N/f$ between the vertical (k) and horizontal (m) wavenumbers.

The unbalanced horizontal velocity components (u_{imb}, v_{imb}) (figure 9*b,c*) show clearly the presence of both the IGW packet and the trapped waves in the vortex interior. The order of magnitude of (u_{imb}, v_{imb}) is 10^{-3} which, taking into account that the horizontal speed during the four inertial periods analysed reached a maximum of 2.0, implies a ratio $O(u_{imb})/O(u) \sim 10^{-3}$.

The above wavenumber, velocity, and frequency relations are consistent with the theory of plane waves which in the plane (x, z), without y-dependence, are complex
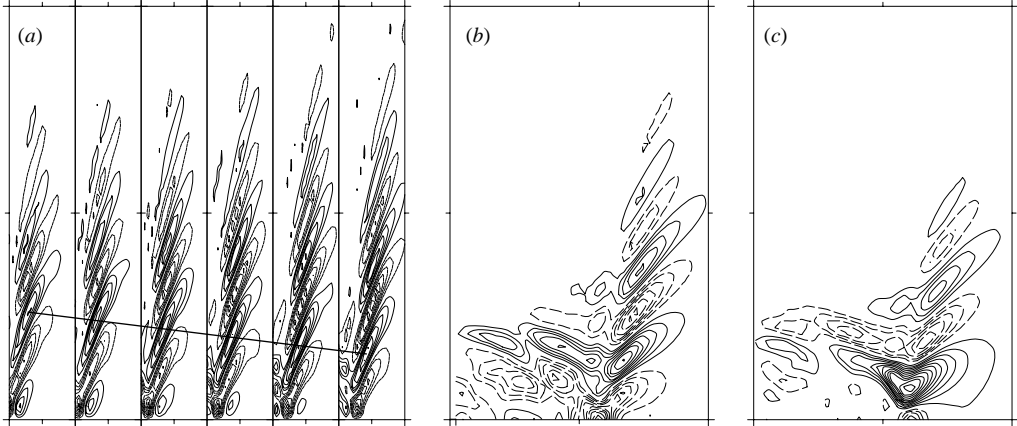
FIGURE 9. (*a*) Time series of w_{imb} (as in figure 7*c*) from $t = 7.3$ to 7.8 i.p. every buoyancy period. The straight thick line connects the same wave crest ($\Delta = 5 \times 10^{-5}$). (*b*, *c*) As in figure 7(*c*) but for the unbalanced horizontal velocity components (*b*) u_{imb} and (*c*) v_{imb} ($\Delta = 5 \times 10^{-4}$). Negative values are dashed (zero contour omitted).

solutions of the form $\tilde{g} = \tilde{g}_0 \exp(i(kx + mz - \omega_p t))$ satisfying the relations

$$\tilde{u} = i\omega_p m k^{-1} \tilde{\mathscr{D}}, \quad \tilde{v} = fmk^{-1}\tilde{\mathscr{D}}, \quad \tilde{w} = -i\omega_p \tilde{\mathscr{D}},$$

where $\tilde{\mathscr{D}}$ is the vertical isopycnal displacement, and the intrinsic frequency ω_p satisfies

$$\omega_p^2 = (f^2 m^2 + N^2 k^2)/(k^2 + m^2).$$

The plane wave solutions therefore predict a ratio $|\tilde{u}_0|/|\tilde{w}_0| = m/k$ between the horizontal and vertical velocity amplitudes of the waves. The maximum velocity amplitudes of the IGW in the packet satisfy $u_{imb}/w_{imb} \simeq 10 = N/f \simeq m/k$. The dispersion relation for plane waves in this case predicts $\omega_p \simeq \sqrt{2}f$, i.e. close to the inertial frequency. Plane wave solutions in the plane (x, z) imply also that $\tilde{u} = i\omega_p \tilde{v}/f \simeq i\sqrt{2}\tilde{v}$, which is consistent both with u_{imb} (figure 9*b*) being larger than v_{imb} (figure 9*c*) and with their observed phase difference, in particular the clockwise rotation of unbalanced horizontal velocity vectors. Differences with the exact plane wave solution are expected since the wave vectors of the localized curved IGW packet change both in magnitude and direction. The average clockwise (*C*) and anticlockwise (*A*) time spectra of the unbalanced horizontal velocity (figure 10*a*) shows the dominance of clockwise rotation at frequencies close to f. The large amplitudes at frequencies smaller than f are attributed to the advection of the wave packet by the background flow. Since this background flow affects both polarities, its effect is partially removed when viewing the ratio $\log(C/A) = \log C - \log A$ (figure 10*a*), which has a clear peak at f. The isopycnal displacement of the unbalanced flow $\mathscr{D}_{imb}$ (proportional to $\nabla \cdot \boldsymbol{\varphi}_{imb}$, not shown) is in phase with u_{imb} but about 10 times smaller, which is also consistent with the plane wave solutions that predict $\tilde{u} = \sqrt{2}N\tilde{\mathscr{D}} = 2\sqrt{2}\pi\tilde{\mathscr{D}}$.

Therefore, consistent with the motion of plane waves in a quasi-hydrostatic flow, the vertical velocity of the simulated IGWs are visible in the distributions of w because the ratio $O(w_{imb})/O(w) = 10^{-4}/10^{-3} = 0.1$. However, the horizontal velocity and the vertical displacement of isopycnals of the IGWs are practically invisible in the distributions of (u, v) and $\mathscr{D}$, respectively, since $O(u_{imb})/O(u) = 10^{-3}/1 = 10^{-3}$ and $O(\mathscr{D}_{imb})/O(\mathscr{D}) = 10^{-4}/10^{-1} = 10^{-3}$. The main differences between the present
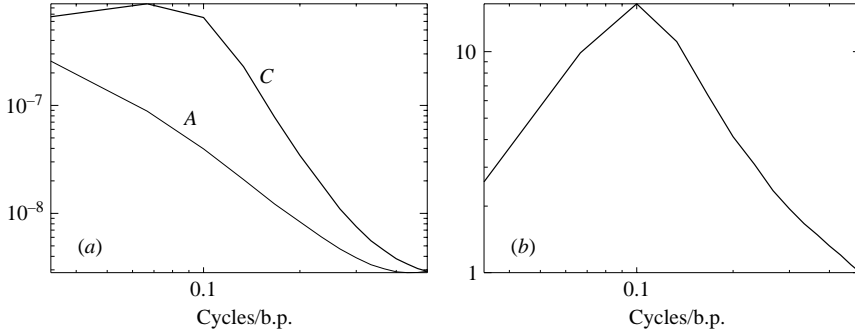
FIGURE 10. (*a*) Clockwise (*C*) and anticlockwise (*A*) frequency spectral components (squared) of the unbalanced horizontal velocity time series, vector $(u_{imb}(\boldsymbol{x}, t_i), v_{imb}(\boldsymbol{x}, t_i))$, with $t_i \in [50, 51, \ldots, 79 \, \mathrm{b.p.}]$. Each spectrum is the average of 128^3 time spectra. (*b*) The ratio C/A.

example and previous examples of SAE (O'Sullivan & Dunkerton 1995; Lane *et al.* 2004; Zhang 2004) include the relatively small amplitude of the IGW packet, the curved IGW phase lines parallel, rather than normal, to the flow, and the upstream propagation of the wave packet.

To conclude, from the unbalanced potential $\boldsymbol{\varphi}_{imb}$ it is possible to identify clearly SAE within a balanced flow, and follow the evolution of small-amplitude IGWs even when the horizontal velocity and vertical displacement of these waves are visually imperceptible in the large-scale balanced flow. The horizontal velocity of the balanced flow is three orders of magnitude larger that the vertical component, which in turn is one order of magnitude larger than the unbalanced vertical velocity. Hence, the OPV balance procedure can feasibly extract unbalanced motions as much as four orders of magnitude smaller than the balanced motions.

3. Concluding remarks

This paper has described a particular way in which a balanced flow spontaneously emits bursts of IGWs. Waves are emitted from a source located at the largest curvature side of the emerging highly ageostrophic anticyclonic vortex in a region of large PV advection. They propagate both outward, or away from the vortex, as a wave packet and inward, where they appear trapped. To observe SAE in this context, where wave amplitudes are exceedingly small, it has been necessary (*a*) to start from a well-balanced, but otherwise ageostrophic and highly time-dependent flow, in this case a strongly unstable baroclinic jet; (*b*) to use sufficient numerical resolution (in this case a grid scale 5×10^{-2} times the width of the jet, or 12.5 grid points per wavelength); and (*c*) to employ an accurate balance–imbalance analysis. Explicit PV conservation is highly advantageous for (*b*) and (*c*).

The results described here open a number of questions. Why is there a highly localized, both in space and in time, IGW packet emission? What triggers the emission of the IGW packet? Can this emission be foreseen (i.e. by monitoring a property of the balanced flow)? Is the source of SAE always in regions of large PV advection, and if so, can a useful criterion be developed? What happens to the trapped waves? What other scenarios are there for SAE, and, in particular, what conditions may enhance SAE and thereby increase the importance of IGWs in geophysical flows?

REFERENCES

BOKHOVE, O. & SHEPERD, T. G. 1996 On Hamiltonian balanced dynamics and the slowest invariant manifold. *J. Atmos. Sci.* **53**, 276–297.

CAMASSA, R. & TIN, S.-K. 1996 The global geometry of the slow manifold in the Lorenz–Krishnamurthy model. *J. Atmos. Sci.* **53**, 3251–3264.

DRITSCHEL, D. G. & VIÚDEZ, A. 2003 A balanced approach to modelling rotating stably stratified geophysical flows. *J. Fluid Mech.* **488**, 123–150.

DRITSCHEL, D. G. & VIÚDEZ, A. 2005 The persistence of balance in geophysical flows. *J. Fluid Mech.* (submitted).

FORD, R., MCINTYRE, M. E. & NORTON, W. A. 2000 Balance and the slow quasimanifold: some explicit results. *J. Atmos. Sci.* **57**, 1236–1254.

GRIFFITHS, M. & REEDER, M. J. 1996 Stratospheric inertia–gravity waves generated in a numerical model of frontogenesis. I: Model solutions. *Q. J. R. Met. Soc.* **122**, 1153–1174.

LANE, T. P., DOYLE, J. D., PLOUGONVEN, R., SHAPIRO, M. A. & SHARMAN, R. D. 2004 Observations and numerical simulations of inertia–gravity waves and shearing instabilities in the vicinity of a jet stream. *J. Atmos. Sci.* **61**, 2692–2706.

LORENZ, E. N. & KRISHNAMURTHY, V. 1987 On the nonexistence of a slow manifold. *J. Atmos. Sci.* **44**, 2940–2950.

O'SULLIVAN, D. & DUNKERTON, T. J. 1995 Generation of inertia–gravity waves in a simulated life cycle of baroclinic instability. *J. Atmos. Sci.* **52**, 3695–3716.

PLOUGONVEN, R., TEITELBAUM, H. & ZEITLIN, V. 2003 Inertia gravity wave generation by the tropospheric midlatitude jet as given by the Fronts and Atlantic Storm-Track Experiment radio sounding. *J. Geophys. Res.–Atmos.* **108**, doi:10.1029/2003JD003535.

PLOUGONVEN, R. & ZEITLIN, V. 2002 Internal gravity wave emission from a pancake vortex: an example of wave–vortex interaction in strongly stratified flows. *Phys. Fluids* **14**, 1259–1268.

SAUJANI, S. & SHEPERD, T. G. 2002 Comments on 'Balance and the slow quasimanifold: some explicit results'. *J. Atmos. Sci.* **59**, 2874–2877. Reply: FORD, R., MCINTYRE, M. E. & NORTON, W. A. 2000 *J. Atmos. Sci.* **59**, 2878–2882.

SNYDER, C., SKAMAROCK, W. C. & ROTUNNO, R. 1993 Frontal dynamics near and following frontal collapse. *J. Atmos. Sci.* **50**, 3194–3211.

VANNESTE, J. 2004 Inertia-gravity wave generation by balanced motion: revisiting the Lorenz–Krishnamurthy model. *J. Atmos. Sci.* **61**, 224–234.

VANNESTE, J. & YAVNEH, I. 2004 Exponentially small inertia–gravity waves and the breakdown of quasigeostrophic balance. *J. Atmos. Sci.* **61**, 211–223.

VIÚDEZ, A. & DRITSCHEL, D. G. 2003 Vertical velocity in mesoscale geophysical flows. *J. Fluid Mech.* **483**, 199–223.

VIÚDEZ, A. & DRITSCHEL, D. G. 2004a Potential vorticity and the quasigeostrophic and semigeostrophic mesoscale vertical velocity. *J. Phys. Oceanogr.* **34**, 865–887.

VIÚDEZ, A. & DRITSCHEL, D. G. 2004b Dynamic potential vorticity initialization and the diagnosis of mesoscale motion. *J. Phys. Oceanogr.* **34**, 2761–2773.

VIÚDEZ, A. & DRITSCHEL, D. G. 2004c Optimal potential vorticity balance of geophysical flows. *J. Fluid Mech.* **521**, 343–352.

WARN, T. 1997 Nonlinear balance and quasi-geostrophic sets. *Atmos. Ocean* **35**, 135–145.

ZHANG, F. 2004 Generation of mesoscale gravity waves in upper-tropospheric jet-front systems. *J. Atmos. Sci.* **61**, 440–457.